doi:10.1038/nature24298

Spectroscopic identification of r-process nucleosynthesis in a double neutron-star merger

E. Pian[1], P. D'Avanzo[2], S. Benetti[3], M. Branchesi[4,5], E. Brocato[6], S. Campana[2], E. Cappellaro[3], S. Covino[2], V. D'Elia[6,7], J. P. U. Fynbo[8], F. Getman[9], G. Ghirlanda[2], G. Ghisellini[2], A. Grado[9], G. Greco[10,11], J. Hjorth[8], C. Kouveliotou[12], A. Levan[13], L. Limatola[9], D. Malesani[8], P. A. Mazzali[14,15], A. Melandri[2], P. Møller[16], L. Nicastro[1], E. Palazzi[1], S. Piranomonte[6], A. Rossi[1], O. S. Salafia[2,17], J. Selsing[8], G. Stratta[10,11], M. Tanaka[18], N. R. Tanvir[19], L. Tomasella[3], D. Watson[8], S. Yang[20,21], L. Amati[1], L. A. Antonelli[6], S. Ascenzi[6,22,23], M. G. Bernardini[2,24], M. Boër[25], F. Bufano[26], A. Bulgarelli[1], M. Capaccioli[9,27], P. Casella[6], A. J. Castro-Tirado[28], E. Chassande-Mottin[29], R. Ciolfi[3,30], C. M. Copperwheat[14], M. Dadina[1], G. De Cesare[1], A. Di Paola[6], Y. Z. Fan[31], B. Gendre[32], G. Giuffrida[6], A. Giunta[6], L. K. Hunt[33], G. L. Israel[6], Z.-P. Jin[31], M. M. Kasliwal[34], S. Klose[35], M. Lisi[6], F. Longo[36], E. Maiorano[1], M. Mapelli[3,37], N. Masetti[1,38], L. Nava[2,39], B. Patricelli[40], D. Perley[14], A. Pescalli[2,41], T. Piran[42], A. Possenti[43], L. Pulone[6], M. Razzano[40], R. Salvaterra[44], P. Schipani[9], M. Spera[3], A. Stamerra[40,45], L. Stella[6], G. Tagliaferri[2], V. Testa[6], E. Troja[46], M. Turatto[3], S. D. Vergani[2,47] & D. Vergani[1]

The merger of two neutron stars is predicted to give rise to three major detectable phenomena: a short burst of γ-rays, a gravitational-wave signal, and a transient optical–near-infrared source powered by the synthesis of large amounts of very heavy elements via rapid neutron capture (the r-process)[1–3]. Such transients, named 'macronovae' or 'kilonovae'[4–7], are believed to be centres of production of rare elements such as gold and platinum[8]. The most compelling evidence so far for a kilonova was a very faint near-infrared rebrightening in the afterglow of a short γ-ray burst[9,10] at redshift $z = 0.356$, although findings indicating bluer events have been reported[11]. Here we report the spectral identification and describe the physical properties of a bright kilonova associated with the gravitational-wave source[12] GW170817 and γ-ray burst[13,14] GRB 170817A associated with a galaxy at a distance of 40 megaparsecs from Earth. Using a series of spectra from ground-based observatories covering the wavelength range from the ultraviolet to the near-infrared, we find that the kilonova is characterized by rapidly expanding ejecta with spectral features similar to those predicted by current models[15,16]. The ejecta is optically thick early on, with a velocity of about 0.2 times light speed, and reaches a radius of about 50 astronomical units in only 1.5 days. As the ejecta expands, broad absorption-like lines appear on the spectral continuum, indicating atomic species produced by nucleosynthesis that occurs in the post-merger fast-moving dynamical ejecta and in two slower (0.05 times light speed) wind regions. Comparison with spectral models suggests that the merger ejected 0.03 to 0.05 solar masses of material, including high-opacity lanthanides.

GW170817 was detected on 17 August 2017, 12:41:04 universal time (UT)[12]. A weak, short-duration ($t \approx 2$ s) γ-ray burst (GRB) in the gravitational-wave error region triggered the Fermi GRB monitor (Fermi-GBM) about two seconds later[13], and was detected also by INTEGRAL SPI-ACS (spectrometer on the International Gamma-Ray Astrophysics Laboratory (INTEGRAL) anticoincidence system)[14] (see also Zhang, B.-B. *et al.*, manuscript in preparation). Considerably improved sky localization was obtained from the joint analysis of LIGO and Virgo data of the gravitational-wave event, with a 90% error region of 33.6 square degrees (ref. 12). This joint gravitational-wave/GRB detection was followed by an extensive worldwide observational campaign using space- and ground-based telescopes to scan the sky region were the events were detected. A new point-like optical source (coordinates right ascension $\alpha(\mathrm{J2000}) = 13\,\mathrm{h}\,09\,\mathrm{min}\,48.09\,\mathrm{s}$, declination $\delta(\mathrm{J2000}) = -23°\,22'\,53.3''$) was soon reported[17,18], located at 10 arcsec from the centre of the S0 galaxy NGC 4993 ($z = 0.00968$; ref. 19) in the ESO 508-G018 group and at a distance of 40 Mpc from Earth, consistent with the luminosity distance of the gravitational-wave signal. It was

[1]INAF, Institute of Space Astrophysics and Cosmic Physics, Via Gobetti 101, I-40129 Bologna, Italy. [2]INAF, Osservatorio Astronomico di Brera, Via E. Bianchi 46, I-23807 Merate, Italy. [3]INAF, Osservatorio Astronomico di Padova, Vicolo dell'Osservatorio 5, I-35122 Padova, Italy. [4]Gran Sasso Science Institute, Viale F. Crispi 7, L'Aquila, Italy. [5]INFN, Laboratori Nazionali del Gran Sasso, I-67100 L'Aquila, Italy. [6]INAF, Osservatorio Astronomico di Roma, Via di Frascati 33, I-00078 Monteporzio Catone, Italy. [7]Space Science Data Center, ASI, Via del Politecnico, 00133 Roma, Italy. [8]Dark Cosmology Centre, Niels Bohr Institute, University of Copenhagen, Juliane Maries Vej 30, DK-2100 Copenhagen Ø, Denmark. [9]INAF, Osservatorio Astronomico di Capodimonte, salita Moiariello 16, I-80131 Napoli, Italy. [10]Università degli Studi di Urbino 'Carlo Bo', Dipartimento di Scienze Pure e Applicate, Piazza Repubblica 13, I-61029 Urbino, Italy. [11]INFN, Sezione di Firenze, I-50019 Sesto Fiorentino, Italy. [12]Astronomy, Physics, and Statistics Institute of Sciences (APSIS) and Department of Physics, The George Washington University, Corcoran Hall, Washington DC 20052, USA. [13]Department of Physics, University of Warwick, Gibbet Hill Road, Coventry CV4 7AL, UK. [14]Astrophysics Research Institute, Liverpool John Moores University, Liverpool Science Park, IC2, 146 Brownlow Hill, Liverpool L3 5RF, UK. [15]Max-Planck-Institut für Astrophysik, Karl-Schwarzschild-Strasse 1, 85748 Garching bei München, Germany. [16]European Southern Observatory, Karl-Schwarzschild-Strasse 2, D-85748 Garching bei München, Germany. [17]Dipartimento di Fisica 'G. Occhialini', Università degli Studi di Milano-Bicocca, Piazza della Scienza 3, I-20126 Milano, Italy. [18]National Astronomical Observatory of Japan, Mitaka, Tokyo, Japan. [19]Department of Physics and Astronomy, University of Leicester, University Road, Leicester LE1 7RH, UK. [20]Department of Astronomy and Physics, Padova University, Padova, Italy. [21]Department of Astronomy, University of California, Davis, California, USA. [22]Dipartimento di Fisica, Università di Roma La Sapienza, Piazzale Aldo Moro 2, I-00185 Rome, Italy. [23]Università di Roma Tor Vergata, Via della Ricerca Scientifica 1, I-00133 Roma, Italy. [24]Laboratoire Univers et Particules de Montpellier, Université Montpellier, CNRS/IN2P3, Montpellier, France. [25]ARTEMIS (UCA, CNRS, OCA), Boulevard de l'Observatoire, CS 34229, F-06304 Nice Cedex 4, France. [26]INAF — Osservatorio Astronomico di Catania, Via S. Sofia 78, I-95123 Catania, Italy. [27]Department of Physics, University of Naples Federico II, Corso Umberto I 40, 80138 Napoli, Italy. [28]Instituto de Astrofisica de Andalucia (CSIC), Glorieta de la Astronomia, E-18008 Granada, Spain. [29]APC, Université Paris Diderot, CNRS/IN2P3, CEA/lrfu, Observatoire de Paris, Sorbonne Paris Cité, France. [30]INFN-TIFPA, Trento Institute for Fundamental Physics and Applications, Via Sommarive 14, I-38123 Trento, Italy. [31]Key Laboratory of Dark Matter and Space Astronomy, Purple Mountain Observatory, Chinese Academy of Science, Nanjing 210008, China. [32]University of Virgin Islands, 2 John Brewer's Bay, St Thomas, Virgin Islands 00802, USA. [33]INAF — Osservatorio Astrofisico di Arcetri, Largo Enrico Fermi 5, I-50125 Florence, Italy. [34]Division of Physics, Mathematics and Astronomy, California Institute of Technology, Pasadena, California 91125, USA. [35]Thüringer Landessternwarte Tautenburg, Sternwarte 5, D-07778 Tautenburg, Germany. [36]University of Trieste and INFN Trieste, I-34127 Trieste, Italy. [37]Institute for Astrophysics and Particle Physics, University of Innsbruck, Technikerstrasse 25/8, A-6020 Innsbruck, Austria. [38]Departamento de Ciencias Fisicas, Universidad Andrés Bello, Fernández Concha 700, Las Condes, Santiago, Chile. [39]INAF, Osservatorio Astronomico di Trieste, Via G.B. Tiepolo 11, I-34143 Trieste, Italy. [40]Scuola Normale Superiore, Piazza dei Cavalieri 7, I-56126 Pisa, Italy. [41]Università degli Studi dell'Insubria, via Valleggio 11, I-22100 Como, Italy. [42]Racah Institute of Physics, The Hebrew University of Jerusalem, Jerusalem 91904, Israel. [43]INAF, Osservatorio Astronomico di Cagliari, Via della Scienza 5, I-09047 Selargius, Italy. [44]INAF, Istituto di Astrofisica Spaziale e Fisica Cosmica di Milano, via E. Bassini 15, I-20133 Milano, Italy. [45]INAF, Osservatorio Astronomico di Torino, Pino Torinese, Italy. [46]NASA, Goddard Space Flight Center, Greenbelt, Maryland 20771, USA. [47]GEPI, Observatoire de Paris, PSL Research University, CNRS, Place Jules Janssen, 92190 Meudon, France.

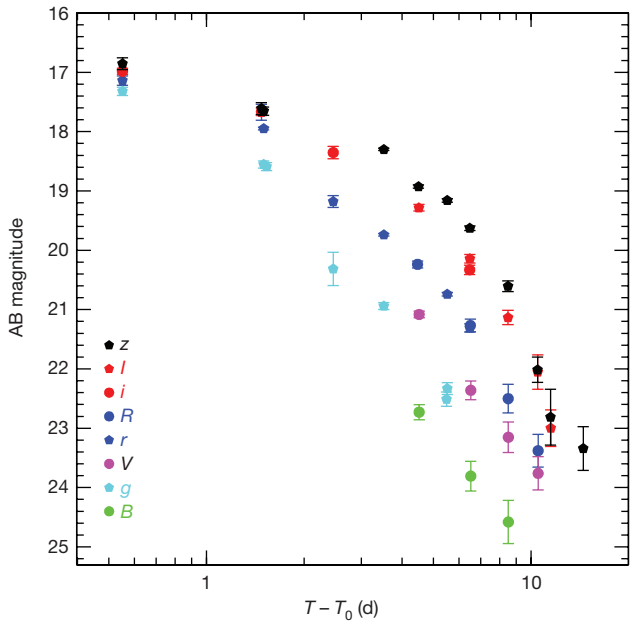

Figure 1 | Multiband optical light curve of AT 2017gfo. The data shown for each filter (see legend) are listed in Extended Data Table 1. Details of data acquisition and analysis are reported in Methods. The x axis indicates the difference in days between the time at which the observation was carried out T and the time of the gravitation-wave event T_0. The error bars show the 1σ confidence level. The data have not been corrected for Galactic reddening.

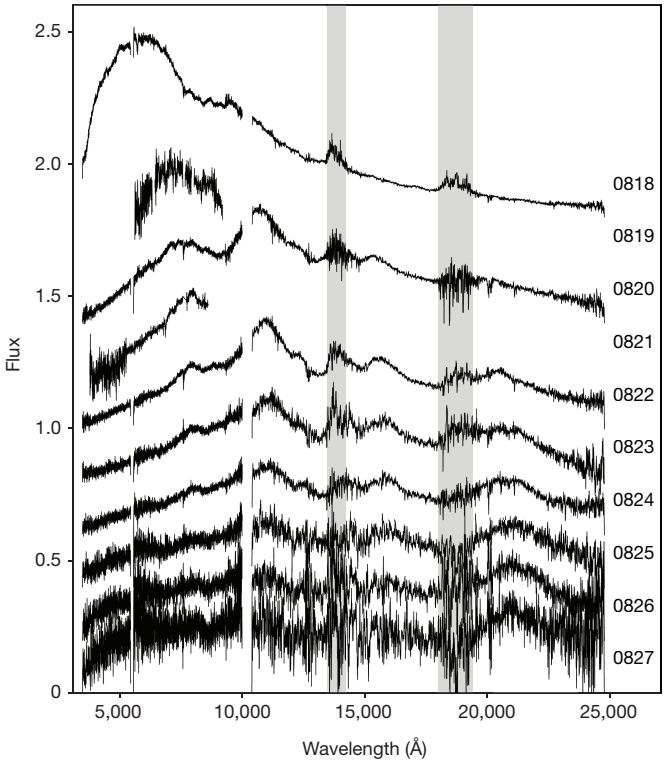

Figure 2 | Time evolution of the AT 2017gfo spectra. VLT/X-shooter, VLT/FORS2 and Gemini/GMOS spectra of AT 2017gfo. Details of data acquisition and analysis are reported in Methods. For each spectrum, the observation epoch is reported on the left (phases with respect to the gravitation-wave trigger time are reported in Extended Data Table 2; the flux normalization is arbitrary). Spikes and spurious features were removed and a filter median of 21 pixels was applied. The shaded areas mark the wavelength ranges with very low atmospheric transmission. The data have not been corrected for Galactic reddening.

first named 'SSS17a' and 'DLT17ck', but here we use the official IAU designation, AT 2017gfo.

We carried out targeted and wide-field optical/near-infrared imaging observations of several bright galaxies within the reconstructed sky localization of the gravitational-wave signal with the Rapid Eye Mount (REM) telescope and with the European Southern Observatory (ESO) Very Large Telescope (VLT) Survey Telescope (ESO-VST). This led to the detection of AT 2017gfo in the REM images of the field of NGC 4993, which were obtained 12.8 h after the gravitational-wave/GRB event. Following the detection of this source, we started an imaging and spectroscopic follow-up campaign at optical and near-infrared wavelengths. Imaging was carried out with the REM telescope, the ESO-VST and the ESO-VLT. A series of spectra was obtained with the VLT/X-shooter in the wavelength range 3,200–24,800 Å, with VLT/FORS2 (Focal Reducer/low-dispersion Spectrograph) in 3,500–9,000 Å and with Gemini-S/GMOS in 5,500–9,000 Å (see ref. 20 for GMOS reduction and analysis details). Overall, we observed the source with an almost daily cadence during the period 17 August 2017 to 3 September 2017 (about 0.5–17.5 days after the gravitational-wave/GRB trigger; details are provided in Methods). We present here the results of the observations carried out in August 2017.

As described in the following, the analysis and modelling of the spectral characteristics of our dataset, together with their evolution with time, result in a good match with the expectations for kilonovae, providing the first compelling observational evidence for the existence of such elusive transient sources. Details of the observations are provided in Methods.

We adopted a foreground Milky Way extinction of $E(B-V)=0.1$ mag and the extinction curve of ref. 21 and used them to correct both magnitudes and spectra (see Methods). The extinction within the host galaxy is negligible according to the absence of substantial detection of characteristic narrow absorption features associated with its interstellar medium. The optical light curve resulting from our data is shown in Fig. 1 and the sequence of X-shooter, FORS2 and GMOS spectra is shown in Fig. 2. Apart from Milky Way foreground lines, the spectrum is otherwise devoid of narrow features that could indicate association with NGC 4993. In the slit, which was displaced from the position of the transient by 3″–10″ (0.6–2.0 kpc in projection), we detected narrow emission lines exhibiting noticeable structure, both spatially and in velocity space (receding at 100–250 km s^{-1} with respect to the systemic velocity), which were probably caused by the slit crossing a spiral structure of the galaxy (see Methods).

The first X-shooter spectrum of the transient shows a bright, blue continuum across the entire wavelength coverage—with a maximum at about 6,000 Å and total luminosity of 3.2×10^{41} erg s^{-1}—that can be fitted with the spectrum of a blackbody of temperature $5{,}000\pm200$ K and a spherical equivalent radius of approximately 8×10^{14} cm. At a phase of 1.5 days after the gravitational-wave/GRB trigger, this indicates an expansion velocity of the ejected material of about $0.2c$. The temperature is considerably lower than that inferred from photometric observations about 20 h earlier (about 8,000 K)[22], suggesting rapid cooling. On top of this overall blackbody spectral shape are undulations that may represent very broad absorption features similar to those predicted by merger ejecta simulations[16]. We refrain from connecting these to the expansion velocity because they may be combinations of many lines with poorly known properties.

At the second epoch, one day later, when the spectrum covered only the optical range, the maximum moved to longer wavelengths, indicating rapid cooling. At the third epoch, when near-infrared wavelength information was again available, the peak shifted further to 11,000 Å and the overall spectral shape changed. This indicated that the photosphere was receding, the ejecta was becoming increasingly transparent and more absorption lines became visible. The near-infrared part of the spectrum evolved in flux and shape much less rapidly than the optical

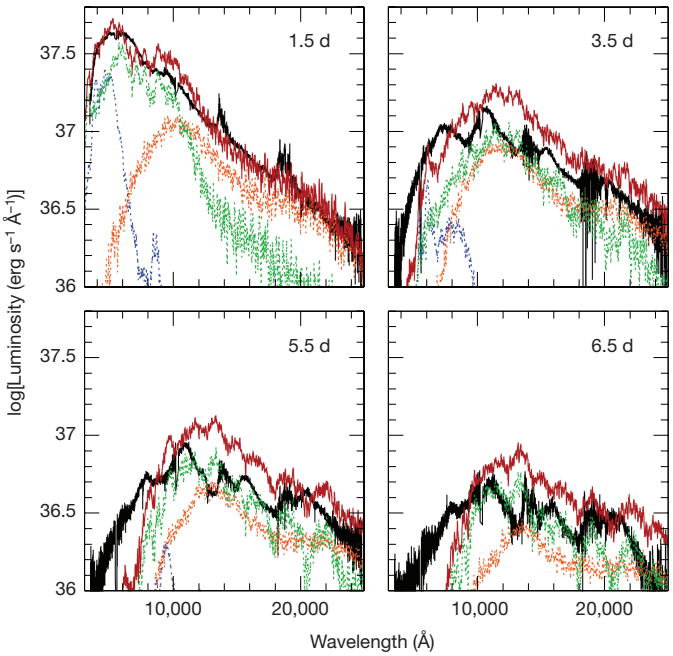

Figure 3 | Kilonova models compared with the AT 2017gfo spectra. X-shooter spectra (black line) at the first four epochs and kilonova models: dynamical ejecta ($Y_e = 0.1$–0.4, orange), wind region with proton fraction $Y_e = 0.3$ (blue) and $Y_e = 0.25$ (green). The red curve represents the sum of the three model components.

part and spectrally broad absorption features ($\Delta\lambda/\lambda \approx 0.1$–$0.2$) were observed. These rapid changes are not consistent with supernova time evolution and are attributed to a kilonova (see Methods and Extended Data Fig. 2).

Unlike supernova absorption lines, the identification of kilonova atomic species is not secure. The neutron-rich environment of the progenitors suggests that r-process nucleosynthesis is the mechanism responsible for the elemental composition of the ejecta. Lacking line identification, we included various plausible nuclear reaction networks in radiation-transfer models of kilonova spectrum formation. A fraction of the synthesized atoms are radioactive; while decaying they heat the ejecta, which then radiates thermally. All the atomic species present in the ejecta have various degrees of excitation and ionization and thus absorb from the continuum and cause the formation of lines. The models that aim at reproducing these lines assume a total explosion energy, a density profile and an abundance distribution of the ejecta. In kilonovae, it is often envisaged that nucleosynthesis takes place in different regions with different neutron excesses and ejecta velocities; typically, a post-merger dynamical ejecta region and a disk-wind region.

Various models predict different emission components and different synthesized masses. Three models with different electron (or proton) fractions Y_e (see Methods) are presented in ref. 16. We compare our spectra with a scenario in which the following three components contribute to the observed spectra (Fig. 3): a lanthanide-rich dynamical ejecta region with a proton fraction in the range $Y_e = 0.1$–0.4 and a velocity of $0.2c$ (orange in Fig. 3), and two slow ($0.05c$) wind regions, one with $Y_e = 0.25$ and mixed (lanthanide-free and lanthanide-rich) composition (green) and one with $Y_e = 0.30$ that is lanthanide-free (blue). Each of these spectra falls short of the observed luminosity by a factor of about 2, while other predictions[5,15] have a discrepancy of an order of magnitude. To investigate the applicability of the model to the present, more luminous spectra than predicted previously, we have assumed that the ejecta mass involved is larger. By decreasing the high-Y_e (0.3) wind component to 30% of the value used in the original model and increasing both the intermediate-Y_e (0.25) wind component and the contribution of the dynamical ejecta nucleosynthesis by a factor of 2, we obtain a satisfactory representation of the first spectrum (Fig. 3).

Although direct rescaling of these models is not in principle correct (for larger masses, we expect that the spectrum of each ejecta could change), we can estimate that the ejected mass was about $0.03M_\odot$–$0.05M_\odot$ and that the high-Y_e-wind ejecta (blue line) is considerably suppressed, possibly because of the viewing angle pointing away from the GRB, a narrow jet angle or both. This also suggests that the ejecta has a wide range of Y_e values, which may vary as a function of latitude.

At each successive epoch, the same components represent the observed spectral features in a less satisfactory way. This indicates that the set of adopted opacities is not completely adequate, as the cooling of the gas is not accompanied by lines of different ionization states, and that the radioactive input may also not be accurately known.

Because a short GRB was detected in association with a gravitational-wave trigger, we evaluated the expected contribution of the GRB afterglow at the epochs of our observations. Nine days after the GW170817 trigger, an X-ray source was discovered by the Chandra X-ray observatory at a position consistent with the kilonova and with a flux of about 4.5×10^{-15} erg cm^{-2} s^{-1} in the energy range 0.3–8 keV. This source could be delayed X-ray afterglow emission from GRB170817A produced by an off-beam jet[23], which may account for the otherwise small probability of having an aligned short-GRB jet within such a small volume[24]. This X-ray emission is consistent with different scenarios: a structured jet with an energy per solid angle decreasing with the angular distance from the axis, viewed at large angles (see, for example, ref. 25), a cocoon accelerated quasi-isotropically at mildly relativistic velocities by the jet[26,27] or a simple uniform jet observed at large angles. All these situations produce an optical afterglow much fainter than that of the kilonova (see Methods). On the other hand, if we assume that the early (0.45 days after the gravitational-wave event) optical flux that we measured is afterglow emission, we estimate an X-ray flux of more than 10^{-12} erg cm^{-2} s^{-1} and a 6-GHz radio flux density of approximately 10 mJy at the same epoch. These estimates are not consistent with the absence of X-ray and radio detections at the corresponding epochs[28,29].

Our long and intensive monitoring and wide range of wavelength coverage allowed the unambiguous detection of time-dependent kilonova emission and full sampling of its time evolution. Our observations not only confirmed the association of the transient with the gravitational wave, but, combined with the short-GRB detection, also proved beyond doubt that at least some short-duration GRBs are indeed associated with compact star mergers. Furthermore, this first detection provides important insights into the environment of merging neutron stars. The location of the gravitational-wave counterpart is only about 2 kpc (projected distance) away from the centre of an early-type galaxy. This offset is typical for short GRBs (see, for example, ref. 30) and is consistent with predictions from theoretical models of merging neutron stars (see, for example, ref. 31). Moreover, the location of the counterpart does not appear to coincide with any globular cluster, which suggests a field origin for this neutron-star binary or a relatively low-velocity ejection from a globular cluster. The nearest possible globular clusters are more than 2.5″ (corresponding to 500 pc) away from the source position[32]. The formation channel of this event could be explored with future modelling and simulations. Finally, since this GRB was rather under-energetic (isotropic γ-ray output of about 10^{46} erg) and probably off-axis with respect to the line of sight, we conclude that there may be a large number of similar nearby off-axis short bursts at frequencies lower than those of γ-rays that are also gravitational-wave emitter candidates but were not followed up. The present event has demonstrated how the search of the randomly oriented parent population of short GRBs can be made effective by coordinated gravitational interferometry and multi-wavelength observations.

Online Content Methods, along with any additional Extended Data display items and Source Data, are available in the online version of the paper; references unique to these sections appear only in the online paper.

Accepted 20 September 2017.

1. Lattimer, J. M., Mackie, F., Ravenhall, D. G. & Schramm, D. N. The decompression of cold neutron star matter. *Astrophys. J.* **213,** 225–233 (1977).
2. Eichler, D., Livio, M., Piran, T. & Schramm, D. Nucleosynthesis, neutrino bursts and gamma-rays from coalescing neutron stars. *Nature* **340,** 126–128 (1989).
3. Li, L.-X. & Paczyński, B. Transient events from neutron star mergers. *Astrophys. J.* **507,** L59–L62 (1998).
4. Kulkarni, S. R. Modelling supernova-like explosions associated with gamma-ray bursts with short durations. Preprint at https://arxiv.org/abs/astro-ph/0510256 (2005).
5. Tanaka, M. & Hotokezaka, K. Radiative transfer simulations of neutron star merger ejecta. *Astrophys. J.* **775,** 113 (2013).
6. Rosswog, S. *et al.* Detectability of compact binary merger macronovae. *Class. Quantum Gravity* **34,** 104001 (2017).
7. Wollaeger, R. T. *et al.* Impact of ejecta morphology and composition on the electromagnetic signatures of neutron star mergers. Preprint at https://arxiv.org/abs/1705.07084 (2017).
8. Metzger, B. D. Kilonovae. *Living Rev. Relativ.* **20,** 3 (2017).
9. Tanvir, N. R. *et al.* A 'kilonova' associated with the short-duration γ-ray burst GRB 130603B. *Nature* **500,** 547–549 (2013).
10. Berger, E., Fong, W. & Chornock, R. An r-process kilonova associated with the short-hard GRB 130603B. *Astrophys. J.* **774,** L23 (2013).
11. Jin, Z.-P. *et al.* The macronova in GRB 050709 and the GRB-macronova connection. *Nat. Commun.* **7,** 12898 (2016).
12. The LIGO Scientific Collaboration and the Virgo Collaboration. GW170817: observation of gravitational waves from a binary neutron star inspiral. *Phys. Rev. Lett.* **119,** 161101 (2017).
13. Goldstein, A. *et al.* An ordinary short gamma-ray burst with extraordinary implications: Fermi-GBM detection of GRB 170817A. *Astrophys. J.* **848,** https://doi.org/10.3847/2041-8213/aa8f41 (2017).
14. Savchenko, V. *et al.* INTEGRAL detection of the first prompt gamma-ray signal coincident with the gravitational event GW170817. *Astrophys. J.* **848,** https://doi.org/10.3847/2041-8213/aa8f94 (2017).
15. Kasen, D., Fernández, R. & Metzger, B. D. Kilonova light curves from the disc wind outflows of compact object mergers. *Mon. Not. R. Astron. Soc.* **450,** 1777–1786 (2015).
16. Tanaka, M. *et al.* Properties of kilonovae from dynamical and post-merger ejecta of neutron star mergers. Preprint at https://arxiv.org/abs/1708.09101 (2017).
17. Coulter, D. A. *et al.* Swope Supernova Survey 2017a (SSS17a), the optical counterpart to a gravitational wave source. *Science* http://doi.org/10.1126/science.aap9811 (2017).
18. Valenti, S. *et al.* The discovery of the electromagnetic counterpart of GW170817: kilonova AT 2017gfo/DLT17ck. *Astrophys. J.* **848,** https://doi.org/10.3847/2041-8213/aa8edf (2017).
19. Jones, D. H. *et al.* The 6dF galaxy survey: final redshift release (DR3) and southern large-scale structures. *Mon. Not. R. Astron. Soc.* **399,** 683–698 (2009).
20. Kasliwal, M. M. *et al.* Illuminating gravitational waves: a concordant picture of photons from a neutron star merger. *Science* http://doi.org/10.1126/science.aap9455 (2017).
21. Cardelli, J. A., Clayton, G. C. & Mathis, J. S. The relationship between infrared, optical, and ultraviolet extinction. *Astrophys. J.* **345,** 245–256 (1989).
22. Malesani, D. *et al.* LIGO/Virgo G298048: optical spectral energy distribution of SSS17a. *GCN Circ.* 21577 (2017).
23. Troja, E. *et al.* The X-ray counterpart to the gravitational-wave event GW170817. *Nature* http://doi.org/10.1038/nature24290 (2017).
24. Patricelli, B. *et al.* Prospects for joint observations of gravitational waves and gamma rays from merging neutron star binaries. *J. Cosmol. Astropart. Phys.* **11,** 56 (2016).
25. Salafia, O. S., Ghisellini, G., Pescalli, A., Ghirlanda, G. & Nappo, F. Structure of gamma-ray burst jets: intrinsic versus apparent properties. *Mon. Not. R. Astron. Soc.* **450,** 3549–3558 (2015).
26. Lazzati, D. *et al.* Off-axis prompt X-ray transients from the cocoon of short gamma-ray bursts. Preprint at https://arxiv.org/abs/1709.01468 (2017).
27. Nakar, E. & Piran, T. The observable signatures of GRB cocoons. *Astrophys. J.* **834,** 28 (2016).
28. Bannister, K. *et al.* LIGO/Virgo G298048: ATCA detection of a radio source coincident with NGC 4993. *GCN Circ.* 21559 (2017).
29. Evans, P. A. *et al.* Swift and NuSTAR observations of GW170817: detection of a blue kilonova. *Science* http://doi.org/10.1126/science.aap9580 (2017).
30. Fong, W. & Berger, E. Hubble Space Telescope observations of short gamma-ray burst host galaxies: morphologies, offsets, and local environments. *Astrophys. J.* **708,** 9–25 (2010).
31. Belczynski, K. *et al.* A study of compact object mergers as short gamma-ray burst progenitors. *Astrophys. J.* **648,** 1110–1116 (2006).
32. Levan, A. J. *et al.* The environment of the binary neutron star merger GW170817. *Astrophys. J.* **848,** https://doi.org/10.3847/2041-8213/aa905f (2017).

Acknowledgements This work is based on observations made with the ESO telescopes at the Paranal Observatory under programmes ID 099.D-0382 (Principal Investigator (PI): E. Pian), 099.D-0622 (PI: P.D'A.), 099.D-0191 (PI: A. Grado) and with the REM telescope at the ESO La Silla Observatory under programme ID 35020 (PI: S. Campana). Gemini observatory data were obtained under programme GS-2017B-DD-1 (PI: L. P. Singer). We thank the Gemini Observatory for performing these observations, the ESO Director General for allocating discretionary time and the ESO operation staff for support. We thank D. Fugazza for technical support with operating the REM telescope remotely and REM telescope director E. Molinari. We acknowledge INAF for supporting the project 'Gravitational Wave Astronomy with the first detections of adLIGO and adVirgo experiments—GRAWITA' (PI: E.B.) and support from ASI grant I/004/11/3. J.H. was supported by a VILLUM FONDEN Investigator grant (project number 16599). M.M.K. acknowledges support from the GROWTH (Global Relay of Observatories Watching Transients Happen) project funded by the National Science Foundation under PIRE grant number 1545949.

Author Contributions E. Pian and P.D'A. coordinated the work. J.S. reduced all the X-shooter spectra presented in Fig. 2 and wrote the relevant sections. M.T. developed the kilonova spectral models. E.C. assisted with the spectral analysis. P.A.M. linked the spectral observations with kilonova theory, coordinated their theoretical interpretation, matched the synthetic with observed spectra (Fig. 3), and wrote the corresponding parts of the paper. S. Campana coordinated the REM observations. S. Covino, A. Grado and A.M. reduced and analysed the optical photometry data (Fig. 1). M.M.K. provided the Gemini spectrum. D.M. assisted with early observation planning. G. Ghirlanda, G. Ghisellini and O.S.S. wrote the section on the off-beam jet (with contributions from L.A., M.G.B., Y.Z.F., Z.-P.J., B.P., T.P. and A.S.). D.W. assisted with the analysis of spectra using thermal models and with writing the paper. E.B. was the PI of the GRAvitational Wave Inaf TeAm (GRAWITA), which works on gravitational-wave electromagnetic follow-up programmes at ESO and other telescopes in Italy and the Canary Islands. M.B. liaised between the GRAWITA and LIGO-Virgo collaborations. A. Grado coordinated the ESO-VST observations. L.L. and F.G. developed the pipeline to reduce the VST data. N.R.T. and A.L. assisted with near-infrared data calibration issues. J.P.U.F., J.H. and C.K. helped write the paper and provided short-GRB expertise. L. Nicastro supervised the data flow and handling. S.P. and V.D. contributed to the data reduction and analysis of the X-shooter spectra. E. Palazzi, A.R., G.S. and G. Greco participated in the organization of the observations and image analysis and provided specific input for photometry calibration. L.T., S.Y. and S.B. contributed to the data analysis, with particular reference to interstellar medium spectral features. P.M. assisted with issues related to ESO policies and observation planning. All GRAWITA members contributed to several phases of the work, from the preparation of proposals, coordination with the LIGO–Virgo collaborations and activation of approved programmes at many facilities to data acquisition, reduction, analysis, interpretation and presentation.

Author Information Reprints and permissions information is available at www.nature.com/reprints. The authors declare no competing financial interests. Readers are welcome to comment on the online version of the paper. Publisher's note: Springer Nature remains neutral with regard to jurisdictional claims in published maps and institutional affiliations. Correspondence and requests for materials should be addressed to E. Pian (pian@iasfbo.inaf.it).

Reviewer Information *Nature* thanks R. Chevalier, C. Miller and the other anonymous reviewer(s) for their contribution to the peer review of this work.

METHODS

Optical/near-infrared imaging. Our first observations of the field of AT 2017gfo were carried out with the 60-cm robotic telescope REM[33], which is located at the ESO La Silla Observatory (Chile), in the *g*, *r*, *i*, *z* and *H* bands from 18 August 2017 01:29:28 UT (12.8 h after the gravitational-wave/GRB event). The field was included in targeted observations of catalogued galaxies in the Ligo–Virgo Collaboration skymap that were aimed at searching for an optical/near-infrared counterpart of the gravitational-wave event and started on 17 August 2017 at 23:11:29 UT (10.5 h after the gravitational-wave/GRB event)[34,35]. Following this first detection, we began an extensive follow-up campaign of optical/near-infrared imaging carried out almost daily for 0.5–17.5 days after the time of the gravitational-wave/GRB trigger. These observations were performed using the ESO VLT, equipped with the X-shooter acquisition camera and the FORS2 instrument, and with the ESO VST, which is equipped with the OmegaCAM instrument[36–39]. The complete record of our photometric observations in August 2017 is presented in Extended Data Table 1. The optical/near-infrared light curves are shown in Fig. 1. For REM and FORS2 images, data reduction was carried out following the standard procedures: subtraction of an averaged bias frame and division by a normalized flat frame. The astrometric solution was computed using the USNO-B1.0 catalogue (http://www.nofs.navy.mil/data/fchpix/). Aperture photometry was performed using SExtractor[40] and the PHOTOM package of the Starlink software (http://starlink.eao.hawaii.edu/starlink). The photometric calibration was achieved by observing the Landolt standard field and using the Pan-STARRS catalogue (https://panstarrs.stsci.edu). To minimize any systematic effect, we performed differential photometry with respect to a selection of local isolated and non-saturated reference stars. As shown in Extended Data Fig. 1, the transient is embedded in the host galaxy light, so that the background around its position is highly inhomogeneous, making accurate photometry measurements arduous. To minimize the effect of flux contamination from the host light, we fitted the transient with an analytical profile. The result obtained from the fit was then subtracted from an image acquired in the neighbourhood of the transient. This procedure was repeated for each frame. After this subtraction, the background around the transient position was much more uniform, enabling accurate photometric measurements. A dedicated procedure was applied for the reduction and analysis of the wide-field images obtained with the VST[41]. The telescope is equipped with OmegaCAM[42], a camera with a field of view of one square degree and 0.21-arcsec pixels. The data were processed with a dedicated pipeline for the VST-OmegaCAM observations (dubbed VST-tube[43]). The pipeline searches for new data in the ESO Data archive and, if available, automatically downloads and processes them by performing the following main steps: pre-reduction, astrometric and photometric calibration and mosaic production. The optical transient magnitude in the AB system is the point-spread-function fitting magnitude measured on the image after subtracting a model of the galaxy obtained fitting the isophotes with the IRAF/STSDAS task ELLIPSE[44]. The reference catalogue APASS DR9 was used for the absolute photometric calibration.

FORS2 spectroscopic observations. FORS2 spectra were acquired with the 600B and 600RI grisms, covering the 3,500–8,600 Å wavelength range fully. In all measurements, we used a 1″ slit to obtain an effective resolution of $R \approx 800$–1,000. Spectral extraction was performed with the IRAF software package (IRAF is the Image Reduction and Analysis Facility made available to the astronomical community by the National Optical Astronomy Observatories, which are operated by AURA, Inc. under contract with the US National Science Foundation; http://iraf.noao.edu). Wavelength and flux calibration of the spectra were performed using helium–argon lamps and spectrophotometric stars. A check for slit losses was carried out by matching the flux-calibrated spectra to our simultaneous photometry data (see Extended Data Tables 1 and 2) and showed that the derived spectral shape is robust.

X-shooter spectroscopic observations. The cross-dispersed echelle spectrograph, X-shooter[45], which is mounted on the VLT, was used to observe the optical/near-infrared counterpart of GW170818. The observing campaign started on the night following the discovery of GW170817 and continued until the source had faded below the detection limit (see Extended Data Table 2) of X-shooter. The observations were carried out using a standard ABBA nodding pattern. Similar position angles of the slit were used for all observations. The position of the slit on the source is shown in Extended Data Fig. 1.

The spectroscopic data obtained with X-shooter were managed with the Reflex interface[46] and reduced using version 2.9.3 of the X-shooter pipeline[47]. The reduction cascade consists of bias subtraction, order tracing, flat fielding, wavelength calibration, flux calibration using the spectrophotometric standard EG274[48], background subtraction and order rectification—all carried out using calibration files obtained nightly. The wavelength solution was refined by cross-correlating the observed sky spectra with a synthetic sky spectrum[49,50], leading to a wavelength solution more accurate than 1 km s^{-1}. Because X-shooter is a cross-dispersed echelle spectrograph, the individual echelle orders are curved across each detector, and a rectification algorithm that correlates neighbouring pixels must be employed. A sampling of 0.2 Å, 0.2 Å or 0.6 Å per pixel (in the ultraviolet B, visible and near-infrared arms, respectively) in the rectified image was chosen to minimize this correlation while conserving the maximal resolving power. The effective resolving power of each observation was obtained from fits to unsaturated telluric absorption lines and yielded mean values of 4,290, 8,150 and 5,750 in the ultraviolet B, visible and near-infrared arms, respectively. These resolving powers are better than the nominal values of the instrument (4,290, 7,410 and 5,410; see https://www.eso.org/sci/facilities/paranal/instruments/xshooter/inst.html) because the seeing point-spread function was narrower than the slit width. Each night, immediately following the observations of the scientific standard, telluric standard stars were also observed, at an airmass comparable to the target airmass. Using the observations of these standard stars, the atmospheric transmission spectrum was obtained using Molecfit[51,52]. Host continuum contamination was visible as a faint background gradient along the slit. To minimize this contamination, we used the background regions closest to the target. The images were combined in nightly sets using a weighting scheme with a moving background variance measure wide enough to avoid the variance measure being pixel-based and, therefore, unsuitable for Poisson-noise-dominated images. For a subset of the observations, the signal-to-noise ratio in the spectral trace was large enough to build a model of the spectral line-spread function and to employ an optimal extraction algorithm[53], but for most of the data, an aperture covering the entire trace was used. To establish an accurate flux calibration, slit loss corrections were calculated using the average seeing full-width at half-maximum of the nightly observations along with the theoretical wavelength dependence of seeing[54]. The slit losses were obtained by integrating a synthetic two-dimensional point-spread function over the width of the slits and corrections were made accordingly.

Foreground dust extinction. We estimated the intervening dust extinction towards the source by using the Na I D line doublet at 5,896 Å. On the basis of the strength of the line in our Galaxy, we derive $E(B-V) = 0.09$ mag using component D1, $E(B-V) = 0.05$ mag using component D2, and $E(B-V) = 0.06$ mag using the sum[55]. The galactic extinction is thus limited to $E(B-V) < 0.1$ mag. Similar upper limits of $E(B-V)$ are obtained from the upper limits of the equivalent widths of the undetected K I 7,699 Å absorption line[56] (<0.025 Å) and of the undetected 8,620 Å diffuse interstellar band[57] (<0.04 Å). These estimates and limits are marginally consistent with the value of $E(B-V) = 0.11$ mag obtained from COBE/DIRBE maps covering that sky region[58].

Spectrum analysis and interpretation. The first-epoch X-shooter spectrum was fitted with the spectrum of a blackbody with temperature of $5{,}000 \pm 200$ K (Extended Data Fig. 2). The main deviations from this fit are two absorption-like lines at 8,100 Å and 12,300 Å that evolve with time and become more pronounced in the second spectrum. At the first epoch, all deviations from the blackbody spectrum are below about 10% in the range 3,500 Å–20,000 Å, indicating that the fit is very satisfactory. Moreover, the expansion speed of $0.2c$ that we derive from the blackbody radius at this epoch (1.5 days) is consistent with the width of the absorption lines that we observe in the second spectrum ($\Delta\lambda/\lambda \approx 0.1$–$0.2$), confirming that the blackbody emission in the first spectrum is highly effective.

The first four X-shooter spectra were compared with calculations by kilonova models[16]. The models use atomic structure calculations for Se ($Z = 34$), Ru ($Z = 44$), Te ($Z = 52$), Ba ($Z = 56$), Nd ($Z = 60$) and Er ($Z = 68$) to construct atomic data for a wide range of r-process elements. By using two different atomic codes, the atomic structure calculations returned opacities that differed from those of the observed spectra by a factor of up to about 2. Multiwavelength radiative-transfer simulations were then used to predict possible variations of kilonova emission. For each model, the abundance in the ejecta was assumed to be homogeneous. However, a high-Y_e component should dominate near the polar region and a low-Y_e/dynamical component should develop in the equatorial region. For each model, the energy release followed a power law ($t^{-1.3}$), where t is the time, owing to the collective effect of the radioactive decay of various nuclei with different lifetimes. The efficiency of the energy deposition was also taken into account, and the energy deposition rate was somewhat steeper than $t^{-1.3}$ because γ-rays can escape without depositing energy.

We emphasize that we have not attempted a real fit of this model to our X-shooter spectra, but have rather looked into an interpretation that is in reasonable agreement with our data. The match is satisfactory for the first X-shooter spectrum, but not for the following three. For this reason, we refrained from deriving a light curve model. In principle, one may fold the synthetic spectral model with the sensitivity curve of any given broad-band filter and integrate the flux in the corresponding band and compare it with the observed one. However, the result may be misleading, regardless of how persuasive it is at face value. Such a spectral comparison allows one to determine the wavelength ranges in which the model is effective and those in which it fails. Integration of the model over a broad wavelength interval cancels the spectral 'memory' and prevents a critical assessment of

the result. In other words, since the spectral model is not completely satisfactory, the comparison of synthetic and observed photometry is not meaningful, although it may seem a good match.

Description of the spectral evolution. The first X-shooter spectrum, obtained at $t = 1.5$ d after the gravitational-wave/GRB trigger, shows an almost featureless, moderately blue continuum. The overall spectral energy distribution is similar to that of early, broad-line core-collapse supernovae. Although at this relatively low temperature (about 5,000 K), supernovae typically show strong broad features, a good match is obtained with the early spectra of the type-Ib supernova SN 2008D/XRF 080109[59] by using the supernova spectral classification tool GELATO[60]. As shown in Extended Data Fig. 2, the X-shooter extended spectral range displays the presence of some large-scale differences from the blackbody fit (dotted line) that are indicative of multi-component contributions, which also suggest a kilonova event.

In the next two days, the spectrum shows a very rapid evolution. The continuum temperature rapidly drops to about 3,300 K, and broad features emerge with peaks at 10,700 Å and 16,000 Å. These broad features point to very high expansion velocity and rapid evolution to a low ejected mass. The combination of the spectral properties and their evolution are unlike those of any known supernova types and are very similar to the predicted outcomes of kilonova models.

In the following week, the temperature derived from the optical continuum seems to remain roughly constant while the peak at 10,700 Å drifts to longer wavelengths (11,200 Å at day 6) and decreases in intensity. Ten days after discovery, the dominant feature in the spectrum is a broad emission centred at about 21,000 Å.

Host galaxy emission analysis. Extending 3″–10″ (0.6–2.0 kpc in projection) from the position of the gravitational-wave counterpart are emission lines formed in the host galaxy. The lines are identified as [O II] $\lambda \approx 3{,}726$ Å and $\lambda \approx 3{,}729$ Å, Hβ, [O III] $\lambda \approx 4{,}959$ Å and $\lambda \approx 5{,}007$ Å, Hα, [N II] $\lambda \approx 6{,}549$ Å and $\lambda \approx 6{,}583$ Å and [S II] $\lambda \approx 6{,}717$ Å and $\lambda \approx 6{,}731$ Å, and they exhibit both spatial and velocity structure along the extent of the slit, as shown in Extended Data Fig. 3.

From the brightest blob of emission, centred at 6″ (1.2 kpc in projection) from the source, we measured a receding velocity of 247 ± 15 km s^{-1} relative to the host nucleus (adopting a systemic velocity of NGC 4993 of $2{,}916 \pm 15$ km s^{-1}). Along the spatial direction of the slit, closer to the source, the emission line centroids become more blue-shifted, approaching a recession velocity of 100 km s^{-1} relative to the NGC 4993 systemic velocity. The velocity range (150 km s^{-1}) of the line emission along the slit indicates coherent motion of the gas along the slit. This is further supported by the dust lanes superposed on the host nucleus[17,61]. The presence of spiral arms was also noted in ref. 62. A strong [N II] $\lambda \approx 6{,}583$ Å line relative to Hα, combined with a weak Hβ relative to [O III] $\lambda \approx 5{,}007$ Å, indicates a radiation field dominated by active galactic nucleus activity, as reported previously[20,63] (see also Cooke, J. *et al.*, manuscript in preparation) and supported by the presence of a central radio source[64]. Using the Balmer decrement, the calculated extinction at the position of the line emission is $E(B-V) = 0.21 \pm 0.21$.

Off-beam jet scenario. GRB170817A had a fluence of 2.2×10^{-7} erg cm^{-2} in the 10–1,000 keV energy range, as observed by the Fermi-GBM. At a distance of 40 Mpc, this fluence corresponds to a γ-ray isotropic equivalent energy $E_{\rm iso} \approx 4.3 \times 10^{46}$ erg. The peak energy is $E_{\rm peak} = 128 \pm 48$ keV (refs 13, 65). The observed $E_{\rm iso}$ is three to four orders of magnitude smaller than the average energy of short GRBs with known redshift[66,67].

For illustration, let us consider a very simple model of a uniform conical jet with semi-aperture angle $\theta_{\rm jet}$ observed off-beam, that is, at a viewing angle $\theta_{\rm view} > \theta_{\rm jet}$. In this case, larger bulk Lorentz factors Γ correspond to larger debeaming factors $b = E_{\rm iso}(0°)/E_{\rm iso}(\theta_{\rm view})$ for a fixed $\theta_{\rm view}$ (refs 68, 69). Given the small distance of 40 Mpc and that the luminosity function probably decreases with increasing luminosity (see, for example, refs 70, 71), we can assume that the on-axis luminosity of this burst belongs to the low-luminosity tail of the luminosity function of the short GRB. For this reason, we assume $E_{\rm iso}(0°) = 10^{50}$ erg, which gives $b = 2{,}500$. The probability of a jet oriented at an angle smaller than $\theta_{\rm view}$ is $P(<\theta_{\rm view}) = 1 - \cos\theta_{\rm view}$. A probability $P > 10\%$ indicates $\theta_{\rm view} > 26°$. An off-axis viewing angle larger than about 30° is also suggested by the expected rate of the joint gravitational-wave and Fermi-GBM detection[24] rescaled to the actual observations. By combining equations (2) and (3) from ref. 68, it is possible to estimate the observed energy $E_{\rm iso}$ and peak energy $E_{\rm peak}$ as a function of $\theta_{\rm view}$ and Γ for a given $\theta_{\rm jet}$. With $\theta_{\rm view} = 30°$, $b = 2{,}500$ ($E_{\rm iso}(0°) = 10^{50}$ erg) requires $\Gamma = 10$ for $\theta_{\rm jet} = 10°$. The latter is consistent with the few existing estimates of short-GRB opening angles[72] and $\Gamma \approx 10$ is within the dispersion limits of the Γ–$E_{\rm iso}$ relation[73,74] for $E_{\rm iso}(0°) \approx 10^{50}$ erg. With these values, $E_{\rm peak}(0°)$ turns out to be approximately 2 MeV and the corresponding comoving-frame peak energy is about 100 keV. If photons with much larger energies were absorbed by pair production, we would expect (as observed at 30°) a spectral cutoff at about 650 keV, which is larger than the peak energy observed by the Fermi-GBM. Although these values of $E_{\rm peak}(0°)$ and $E_{\rm iso}(0°)$ are consistent with those observed in short GRBs, they locate this burst relatively far from the possible spectral energy correlations of short GRBs.

Extended Data Fig. 4 shows the predicted afterglow light curves at 6 GHz, the R-band and 1 keV. The filled circle shows the X-ray flux at 15 days after the gravitational-wave/GRB trigger[23,75]. The arrows show two representative radio upper limits: at 8.65 days (obtained[76] by adding together six e-MERLIN observations at 5 GHz) and at 20 days (obtained[77] with MeerKAT at 1.5 GHz). To obtain the model curves, we assumed the parameters $\theta_{\rm jet} = 10°$, $\theta_{\rm view} = 30°$, isotropic-equivalent kinetic energy $E_{\rm k,iso} = 10^{50}$ erg, $\Gamma = 10$, an interstellar medium with uniform density $n = 2 \times 10^{-3}$ cm^{-3} and standard micro-physical parameters at the shock, that is, $\varepsilon_{\rm e} = 0.1$, $\varepsilon_{\rm B} = 0.01$ (where $\varepsilon_{\rm e}$ and $\varepsilon_{\rm B}$ are the fraction of shock energy carried by the electrons and by the magnetic field, respectively) and electron energy injection power-law index $p = 2.1$. We used standard afterglow dynamics and radiation codes[78]. As can be seen, the R flux is always below 2×10^{-5} mJy, corresponding to $R > 28$, and therefore orders of magnitude lower than kilonova emission.

Data availability. The data presented in this paper and supporting the findings of this study are available from the corresponding author on reasonable request.

33. Chincarini, G. *et al.* The last born at La Silla: REM, the Rapid Eye Mount. *Messenger* **113,** 40–44 (2003).
34. Melandri, A. *et al.* LIGO/Virgo G298048: REM optical/NIR observations of candidate in NGC 4993. *GCN Circ.* 21532 (2017).
35. Melandri, A. *et al.* LIGO/Virgo G298048: REM optical/NIR observations. *GCN Circ.* 21556 (2017).
36. Pian, E. *et al.* LIGO/Virgo G298048: GRAWITA VLT/X-shooter observations and tentative redshift of SSS17a. *GCN Circ.* 21592 (2017).
37. D'Avanzo, P. *et al.* LIGO/Virgo G298048: ESO/VLT optical observations. *GCN Circ.* 21653 (2017).
38. Grado, A. *et al.* LIGO/VIRGO G298048: INAF VST-ESO PARANAL observations. *GCN Circ.* 21598 (2017).
39. Grado, A. *et al.* LIGO/VIRGO G298048: INAF VST-ESO PARANAL observations of NGC4993. *GCN Circ.* 21703 (2017).
40. Bertin, E. & Arnouts, S. SExtractor: software for source extraction. *Astron. Astrophys. Suppl. Ser.* **117,** 393–404 (1996).
41. Capaccioli, M. & Schipani, P. The VLT survey telescope opens to the sky: history of a commissioning. *Messenger* **146,** 2–7 (2011).
42. Kuijken, K. OmegaCAM: ESO's newest imager. *Messenger* **146,** 8–11 (2011).
43. Grado, A., Capaccioli, M., Limatola, L. & Getman, F. VST processing facility: first astronomical applications. *Mem. Soc. Astron. It. Suppl.* **19,** 362 (2012).
44. Tody, D. IRAF in the Nineties. In *Astronomical Data Analysis Software and Systems II* (eds Hanisch, R. J. *et al.*) 173–183 *(ASP Conf. Ser.* Vol. 52, 1993).
45. Vernet, J. *et al.* X-shooter, the new wide band intermediate resolution spectrograph at the ESO Very Large Telescope. *Astron. Astrophys.* **536,** A105 (2011).
46. Freudling, W. *et al.* Automated data reduction workflows for astronomy. The ESO Reflex environment. *Astron. Astrophys.* **559,** A96 (2013).
47. Modigliani, A. *et al.* The X-shooter pipeline. *Proc. SPIE* **7737,** http://doi.org/10.1117/12.857211 (2010).
48. Moehler, S. *et al.* Flux calibration of medium-resolution spectra from 300 nm to 2500 nm: model reference spectra and telluric correction. *Astron. Astrophys.* **568,** A9 (2014).
49. Noll, S. *et al.* An atmospheric radiation model for Cerro Paranal. I. The optical spectral range. *Astron. Astrophys.* **543,** A92 (2012).
50. Jones, A. *et al.* An advanced scattered moonlight model for Cerro Paranal. *Astron. Astrophys.* **560,** A91 (2013).
51. Smette, A. *et al.* Molecfit: a general tool for telluric absorption correction. I. Method and application to ESO instruments. *Astron. Astrophys.* **576,** A77 (2015).
52. Kausch, W. *et al.* Molecfit: a general tool for telluric absorption correction. II. Quantitative evaluation on ESO-VLT/X-Shooter spectra. *Astron. Astrophys.* **576,** A78 (2015).
53. Horne, W. An optimal extraction algorithm for CCD spectroscopy. *Publ. Astron. Soc. Pac.* **98,** 609–617 (1986).
54. Fried, D. L. Limiting resolution looking down through the atmosphere. *J. Opt. Soc. Am.* **56,** 1380–1384 (1966).
55. Poznanski, D., Prochaska, J. X. & Bloom, J. S. An empirical relation between sodium absorption and dust extinction. *Mon. Not. R. Astron. Soc.* **426,** 1465–1474 (2012).
56. Munari, U. & Zwitter, T. Equivalent width of Na I and K I lines and reddening. *Astron. Astrophys.* **318,** 269–274 (1997).
57. Munari, U. *et al.* Diffuse interstellar bands in RAVE survey spectra. *Astron. Astrophys.* **488,** 969–973 (2008).
58. Schlafly, E. F. & Finkbeiner, D. P. Measuring reddening with Sloan Digital Sky Survey stellar spectra and recalibrating SFD. *Astrophys. J.* **737,** 103 (2011).
59. Mazzali, P., Valenti, S. & Della Valle, M. The metamorphosis of supernova SN 2008D/XRF 080109: a link between supernovae and GRBs/hypernovae. *Science* **321,** 1185–1188 (2008).
60. Harutyunyan, A. *et al.* ESC supernova spectroscopy of non-ESC targets. *Astron. Astrophys.* **488,** 383–399 (2008).
61. Pan, Y.-C. The old host-galaxy environment of SSS17a, the first electromagnetic counterpart to a gravitational-wave source. *Astrophys. J.* **848,** https://doi.org/10.3847/2041-8213/aa9116 (2017).

62. Levan, A. J. *et al.* LIGO/Virgo G298048: MUSE Integral field observations. *GCN Circ*. 21681 (2017).
63. Hallinan, G. *et al.* A radio counterpart to a neutron star merger. *Science* http://doi.org/10.1126/science.aap9855 (2017).
64. Alexander, K. D. *et al.* The electromagnetic counterpart of the binary neutron star merger LIGO/VIRGO GW170817. VI. Radio constraints on a relativistic jet and predictions for late-time emission from the kilonova ejecta. *Astrophys. J.* **848,** https://doi.org/10.3847/2041-8213/aa905d (2017).
65. Goldstein, A. *et al.* LIGO/Virgo G298048: update on Fermi/GBM GRB 170817A analysis. *GCN Circ*. 21528 (2017).
66. D'Avanzo, P. *et al.* A complete sample of bright Swift short gamma-ray bursts. *Mon. Not. R. Astron. Soc.* **442,** 2342–2356 (2014).
67. Berger, E. Short-duration gamma-ray bursts. *Annu. Rev. Astron. Astrophys.* **52,** 43–105 (2014).
68. Ghisellini, G. *et al.* Are GRB980425 and GRB031203 real outliers or twins of GRB060218? *Mon. Not. R. Astron. Soc.* **372,** 1699–1709 (2006).
69. Salafia, O. S., Ghisellini, G., Pescalli, A., Ghirlanda, G. & Nappo, F. Light curves and spectra from off-axis gamma-ray bursts. *Mon. Not. R. Astron. Soc.* **461,** 3607–3619 (2016).
70. Wanderman, D. & Piran, T. The rate, luminosity function and time delay of non-collapsar short GRBs. *Mon. Not. R. Astron. Soc.* **448,** 3026–3037 (2015).
71. Ghirlanda, G. *et al.* Short gamma-ray bursts at the dawn of the gravitational wave era. *Astron. Astrophys.* **594,** A84 (2016).
72. Fong, W. *et al.* The afterglow and early-type host galaxy of the short GRB 150101B at $z = 0.1343$. *Astrophys. J.* **833,** 151 (2016).
73. Ghirlanda, G. *et al.* Gamma-ray bursts in the comoving frame. *Mon. Not. R. Astron. Soc*. **420,** 483–494 (2012).
74. Liang, E.-W. *et al.* A comprehensive study of gamma-ray burst optical emission. II. Afterglow onset and late re-brightening components. *Astrophys. J.* **774,** 13 (2013).
75. Haggard, D. *et al.* A deep Chandra X-ray study of neutron star coalescence GW170817. *Astrophys. J.* **848,** https://doi.org/10.3847/2041-8213/aa8ede (2017).
76. Moldon, J. & Beswick, R. LIGO/Virgo G298048: e-MERLIN upper limits on 5 GHz compact emission from SSS17a. *GCN Circ*. 21804 (2017).
77. Mooley, K. *et al.* LIGO/VIRGO G298048: MeerKAT observations of SSS17a. *GCN Circ*. 21891 (2017).
78. van Eerten, H. J., Leventis, K., Meliani, Z., Wijers, R. A. M. J. & Keppens, R. Gamma-ray burst afterglows from transrelativistic blast wave simulations. *Mon. Not. R. Astron. Soc*. **403,** 300–316 (2010).

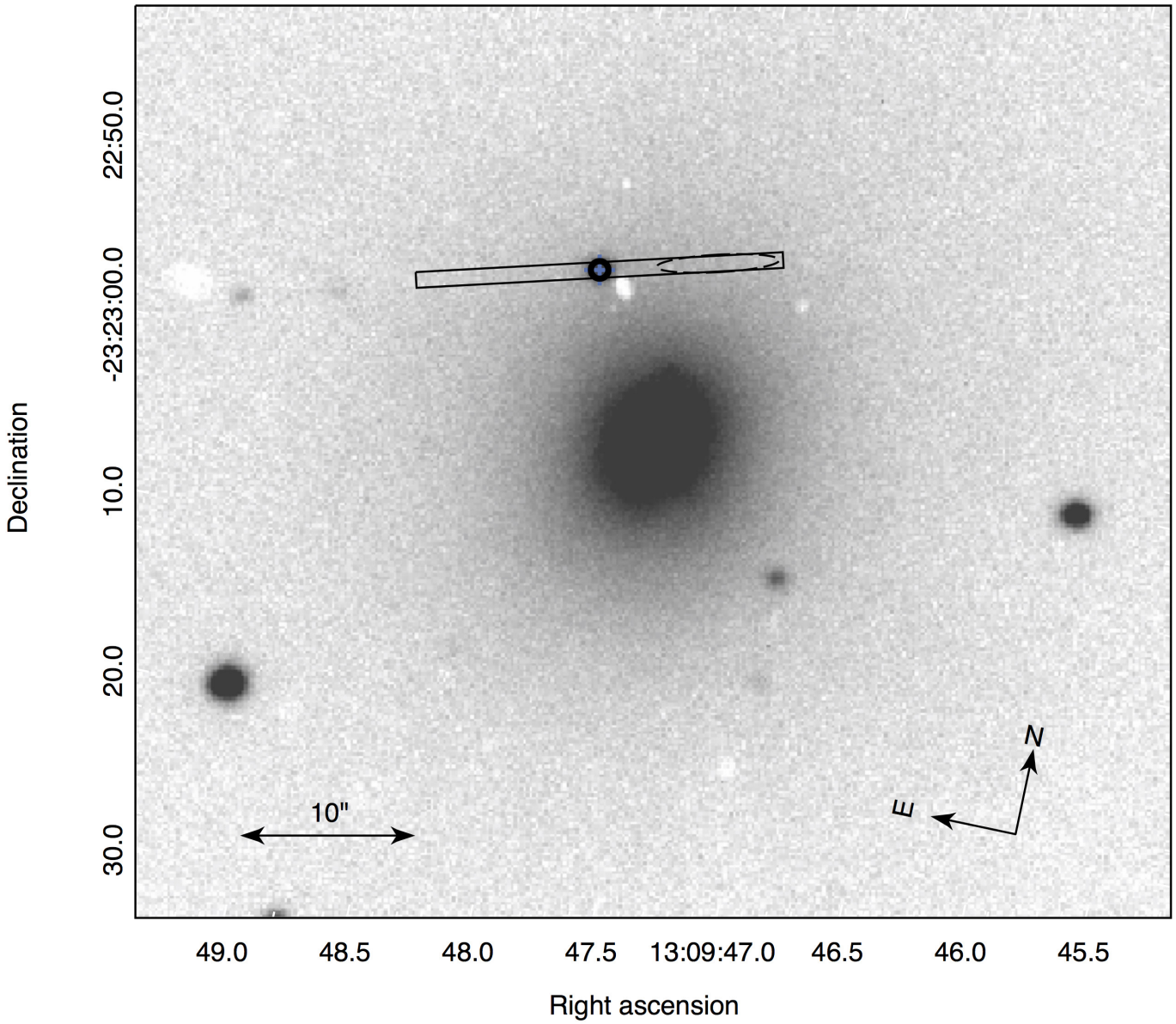

Extended Data Figure 1 | Image of the NGC 4993 galaxy . The image was obtained with the X-shooter acquisition camera (*z* filter). The X-shooter slit is overlaid as a rectangle. The position of the optical transient is marked by a blue circle. The position of the line emission in the slit is marked by an ellipse. The dust lanes that are visible in the host intersect the slit at the position of the line emission.

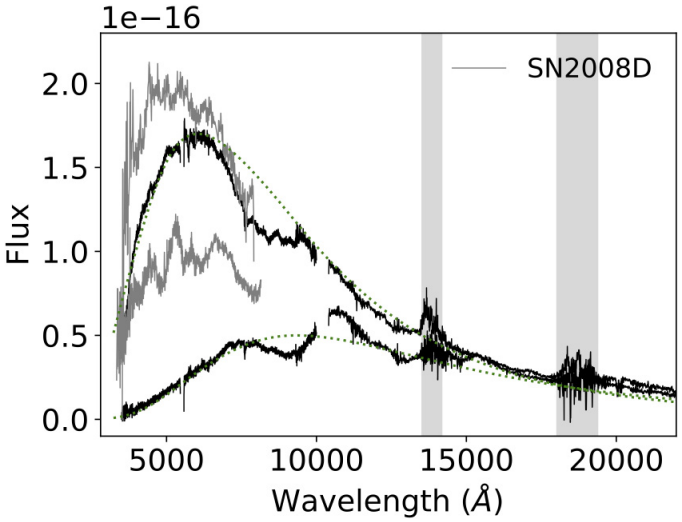

Extended Data Figure 2 | Blackbody fit to the AT 2017gfo spectra. The two early X-shooter spectra of GW170817, obtained 1.5 and 3.5 days after discovery, are compared with the spectra of the type-Ib supernova SN 2008D[59], obtained 2–5 days after the explosion (light grey, arbitrarily scaled in flux, $\times 10^{-16}$). The shaded areas represent wavelength intervals with low atmospheric transmission. The dotted green lines show the blackbody fits of the optical continuum of GW170817 with temperature 5,000 K and 3,200 K.

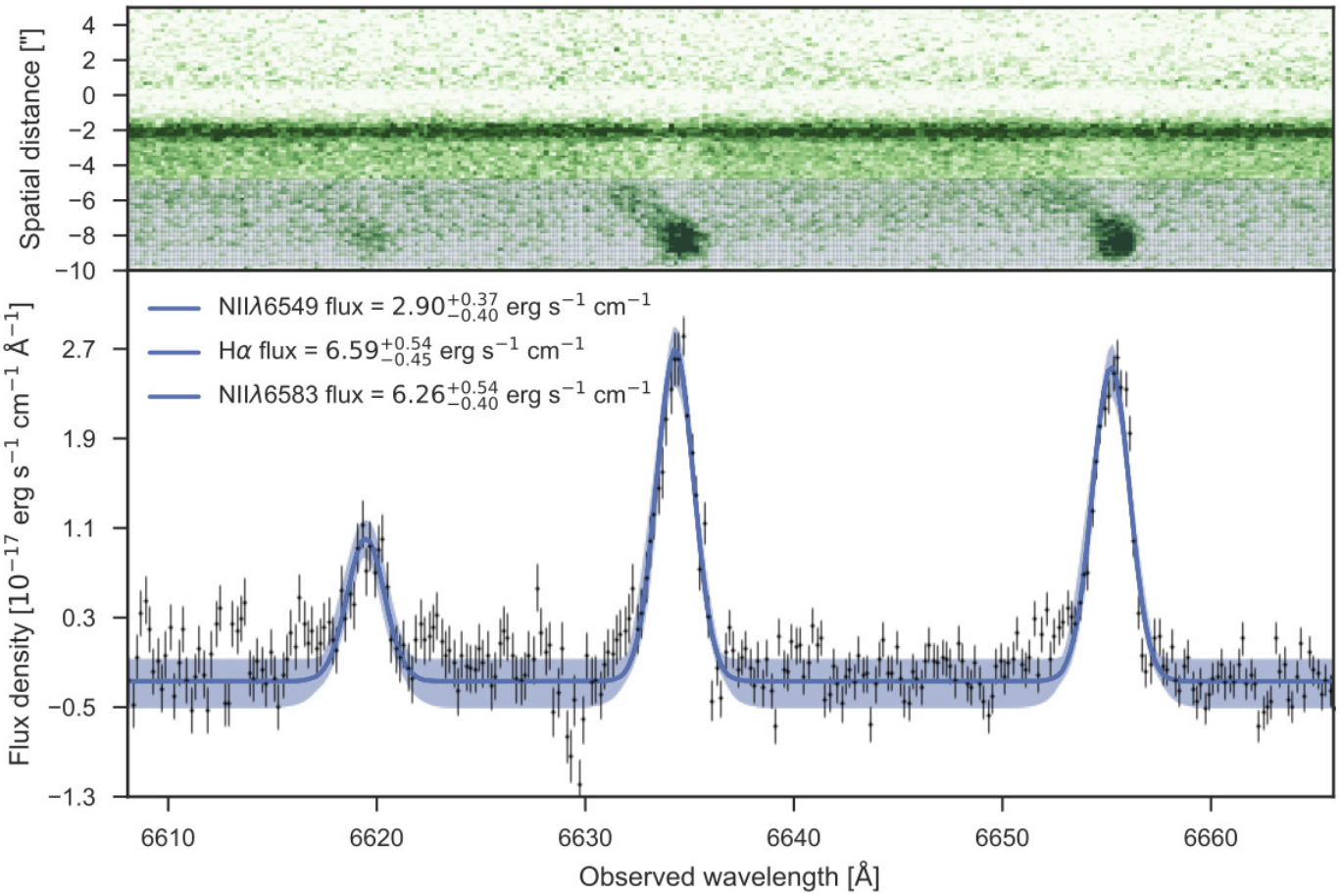

Extended Data Figure 3 | Two-dimensional image of the AT 2017gfo spectrum. Top, the rectified, X-shooter two-dimensional image. The dark line visible across the entire spectral window is the bright continuum of the optical transient and the offset. The dark green blobs indicate the position of the line emission from N II $\lambda \approx 6{,}549$ Å, Hα and N II $\lambda \approx 6{,}583$ Å. Bottom, the line emission and the line fits. The integrated line fluxes are given, normalized by a factor of 10^{-17} for clarity. The error bars on the black points represent the individual 1σ spectral uncertainties. The blue shaded area represents 1σ uncertainty.

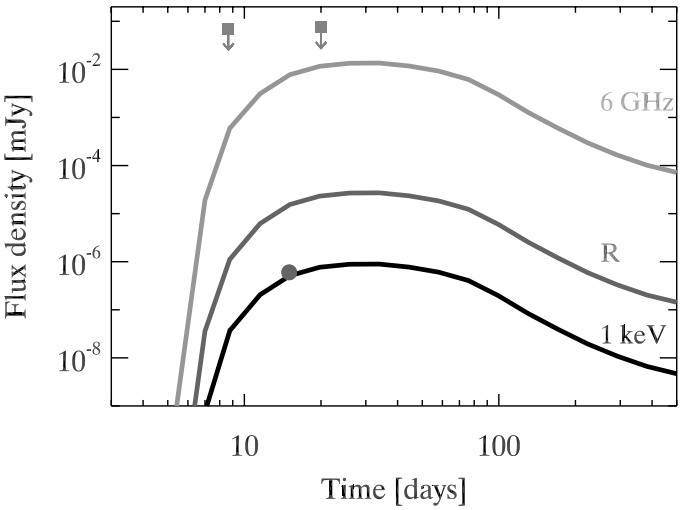

Extended Data Figure 4 | Off-axis GRB afterglow model. Synthetic X-ray (black curve), optical (dark grey curve) and radio (light grey curve) light curves of the GRB afterglow, as predicted by an off-axis jet model, derived using standard afterglow dynamics and radiation codes[78]. The filled circle shows the X-ray detection[23] and the squares with arrows show two representative radio upper limits[76,77].

Extended Data Table 1 | Log of photometric observations

MJD[a]	Phase[b] (days)	Telescope	Instrument	Exposure (seconds)	Filter	Mag[c]
57987.02	4.5	VLT	FORS2	480	*B*	22.729 ± 0.128
57989.02	6.5	VLT	FORS2	600	*B*	23.807 ± 0.251
57991.01	8.5	VLT	FORS2	600	*B*	24.581 ± 0.363
57983.05	0.5	REM	ROS2	720	*g*	17.320 ± 0.070
57984.00	1.5	VLT	XS	90	*g*	18.553 ± 0.060
57984.03	1.5	REM	ROS2	720	*g*	18.591 ± 0.068
57984.96	2.5	REM	ROS2	720	*g*	20.314 ± 0.282
57986.02	3.5	VLT	XS	90	*g*	20.940 ± 0.060
57987.99	5.5	VST	OmegaCam	200	*g*	22.507 ± 0.122
57988.02	5.5	VLT	XS	90	*g*	22.332 ± 0.100
57987.02	4.5	VLT	FORS2	240	*V*	21.082 ± 0.054
57989.02	6.5	VLT	FORS2	600	*V*	22.361 ± 0.158
57991.01	8.5	VLT	FORS2	600	*V*	23.152 ± 0.256
57993.01	10.5	VLT	FORS2	840	*V*	23.761 ± 0.280
57983.05	0.5	REM	ROS2	720	*r*	17.140 ± 0.080
57983.98	1.5	REM	ROS2	720	*r*	17.675 ± 0.134
57984.00	1.5	VLT	XS	90	*r*	17.951 ± 0.020
57984.96	2.5	REM	ROS2	720	*r*	19.178 ± 0.100
57986.02	3.5	VLT	XS	90	*r*	19.740 ± 0.020
57986.97	4.5	VLT	FORS2	240	*R*	20.238 ± 0.058
57988.02	5.5	VLT	XS	90	*r*	20.740 ± 0.030
57988.98	6.5	VST	OmegaCam	200	*r*	21.310 ± 0.075
57989.00	6.5	VLT	FORS2	240	*R*	21.268 ± 0.106
57991.00	8.5	VLT	FORS2	240	*R*	22.501 ± 0.240
57993.01	10.5	VLT	FORS2	360	*R*	23.379 ± 0.277
57983.05	0.5	REM	ROS2	720	*i*	16.984 ± 0.050
57983.98	1.5	REM	ROS2	720	*i*	17.664 ± 0.064
57984.96	2.5	REM	ROS2	720	*i*	18.354 ± 0.105
57987.01	4.5	VLT	FORS2	300	*I*	19.284 ± 0.055
57988.97	6.5	VST	OmegaCam	200	*i*	20.329 ± 0.089
57988.98	6.5	VLT	FORS2	300	*I*	20.142 ± 0.072
57990.99	8.5	VLT	FORS2	300	*I*	21.133 ± 0.119
57992.99	10.5	VLT	FORS2	300	*I*	22.052 ± 0.289
57994.00	11.5	VLT	FORS2	630	*I*	23.000 ± 0.309
57983.05	0.5	REM	ROS2	720	*z*	16.854 ± 0.100
57983.98	1.5	REM	ROS2	720	*z*	17.611 ± 0.098
57984.00	1.5	VLT	XS	90	*z*	17.654 ± 0.070
57986.02	3.5	VLT	XS	90	*z*	18.300 ± 0.020
57987.00	4.5	VLT	FORS2	300	*z*	18.927 ± 0.027
57988.02	5.5	VLT	XS	90	*z*	19.160 ± 0.030
57988.98	6.5	VLT	FORS2	300	*z*	19.627 ± 0.039
57990.99	8.5	VLT	FORS2	300	*z*	20.606 ± 0.092
57992.98	10.5	VLT	FORS2	600	*z*	22.014 ± 0.214
57993.98	11.5	VLT	FORS2	720	*z*	22.815 ± 0.471
57996.98	14.5	VLT	FORS2	1350	*z*	23.342 ± 0.368

[a]Julian day, JD − 2400000.5.
[b]After the time of the gravitational-wave/GRB trigger.
[c]AB magnitudes, not corrected for galactic extinction.

Extended Data Table 2 | Log of spectroscopic observations

UT[a]	MJD[b]	Phase[c] (days)	Instrument	Slit/Grism (arcsec)	Exp.Time (s)	Airmass (min/max)	Seeing (arcsec)	F^{d}_{Vis}	F^{d}_{NIR}
18.97	57983.97	1.5	VLT/X-shooter	1.0/0.9/0.9	2400	1.45/1.72	0.61	166	40
19.95	57984.95	2.5	Gemini-S/GMOS	–	600	2.5/2.7	–	53	–
20.98	57985.98	3.5	VLT/X-shooter	1.0/0.9/0.9	3600	1.52/2.12	0.9	27.8	36.5
21.98	57986.98	4.5	VLT/FORS2	600RI	1800	1.58/1.86	0.88	18	-
22.03	57987.03	4.5	VLT/FORS2	600B	700	2.60/2.91	0.59	18	-
22.98	57987.98	5.5	VLT/X-shooter	1.0/0.9/0.9	3600	1.58/2.25	0.71	10.8	23.9
23.98	57988.98	6.5	VLT/X-shooter	1.0/0.9/0.9	3600	1.74/2.33	0.87	7.0	15.4
24.98	57989.98	7.5	VLT/X-shooter	1.0/0.9/0.9	3600	1.66/2.44	0.53	6.3	12
25.98	57990.98	8.5	VLT/X-shooter	1.0/0.9/0.9	2400	1.74/1.98	0.65	6.1	8.2
26.97	57991.97	9.5	VLT/X-shooter	1.0/0.9/0.9	3600	1.69/2.50	0.78	5.1	6.0
27.97	57992.97	10.5	VLT/X-shooter	1.0/0.9/0.9	3600	1.70/2.53	0.67	4.7	4.5

[a]UT days of August 2017.
[b]JD − 2400000.5.
[c]After the time of the gravitational-wave/GRB trigger.
[d]Fluxes at 6,000 Å and 15,000 Å in 10^{-18} erg s^{-1} cm^{-2} $Å^{-1}$, not corrected for reddening; uncertainties are about 10%.